

# Geochemistry, Geophysics, Geosystems

## RESEARCH ARTICLE

10.1029/2020GC009172

### Key Points:

- An open-source Transdimensional Hierarchical Bayesian (THB) inversion code can resolve seismic structure and measurement uncertainty from active source seismic refraction surveys
- Comprehensive synthetic tests demonstrate the reliability of using seismic refraction for critical zone research
- A field survey with THB inversion shows changes of weathering structure thickness in a ridge-channel system landscape

### Supporting Information:

Supporting Information may be found in the online version of this article.

### Correspondence to:

M.-H. Huang,  
mhhuang@umd.edu






### Citation:

Huang, M.-H., Hudson-Rasmussen, B., Burdick, S., Lekic, V., Nelson, M. D., Fauria, K. E., & Schmerr, N. (2021). Bayesian seismic refraction inversion for critical zone science and near-surface applications. *Geochemistry, Geophysics, Geosystems*, 22, e2020GC009172. <https://doi.org/10.1029/2020GC009172>

Received 12 MAY 2020

Accepted 15 MAR 2021

## Bayesian Seismic Refraction Inversion for Critical Zone Science and Near-Surface Applications

Mong-Han Huang<sup>1</sup> , Berit Hudson-Rasmussen<sup>1,2</sup> , Scott Burdick<sup>3</sup>, Vedran Lekic<sup>1</sup> , Mariel D. Nelson<sup>4</sup>, Kristen E. Fauria<sup>5</sup> , and Nicholas Schmerr<sup>1</sup> 
<sup>1</sup>Department of Geology, University of Maryland, College Park, MD, USA, <sup>2</sup>Department of Geology, Carleton College, Northfield, MN, USA, <sup>3</sup>College of Liberal Arts and Sciences, Wayne State University, Detroit, MI, USA, <sup>4</sup>Department of Geological Sciences, University of Texas at Austin, Austin, TX, USA, <sup>5</sup>Department of Earth and Environmental Sciences, Vanderbilt University, Nashville, TN, USA

**Abstract** The critical zone (CZ) is the region of the Earth's surface that extends from the bottom of the weathered bedrock to the tree canopy and is important because of its ability to store water and support ecosystems. A growing number of studies use active source shallow seismic refraction to explore and define the size and structure of the CZ across landscapes. However, measurement uncertainty and model resolution at depth are generally not evaluated, which makes the identification and interpretation of CZ features inconclusive. To reliably resolve seismic velocity with depth, we implement a Transdimensional Hierarchical Bayesian (THB) framework with reversible-jump Markov Chain Monte Carlo to generate samples from the posterior distribution of velocity structures. We also perform 2D synthetic tests to explore how well THB traveltime inversion can resolve different subsurface velocity structures. We find that THB recovers both sharp changes in velocity as well as gradual velocity increases with depth. Furthermore, we explore the velocity structure in a series of ridge-valley systems in northern California. The posterior velocity model shows an increasing thickness of low velocity material from channels to ridgetops along a transect parallel to bedding strike, implying a deeper weathering zone below ridgetops and hillslopes than below channels. The THB method enhances the ability to reliably image CZ structure, and the model uncertainty estimates it yields provides an objective way to interpret deep CZ structure. The method can be applied across other near-surface studies, especially in the presence of significant surface topography.

## 1. Introduction

The critical zone (CZ) refers to the region between fresh bedrock, which is meters to tens of meters below ground surface, and the tree canopy (National Research Council [NRC], 2001; Riebe et al., 2017). The CZ is essential to life because of its ability to store water and support ecosystems on Earth. As summarized by Riebe et al. (2017), several studies have hypothesized how subsurface CZ structure varies along hillslopes and is influenced by different geology, tectonic, and climate conditions (e.g., Anderson et al., 2013; Lebedeva & Brantley, 2013; Rempe & Dietrich, 2014; St. Clair et al., 2015). Two common CZ models describe subsurface CZ structures in a ridge-channel system as regulated by either regional stress or hydrology (Figures 1a and 1c). Accurately resolving CZ structure in a range of field settings will be critical to testing these and other process-based models.

Measuring CZ structure is not trivial, mainly because the depth to unweathered bedrock is often tens of meters below surface (Holbrook et al., 2014) and cannot be accessed directly. Common approaches such as drilling are expensive, whereas digging soil pits and augering are time consuming. Moreover, these methods only provide point measurements and cannot efficiently map CZ variations at watershed scales. On steep hillslopes, using these methods can also be logistically challenging.

Seismic imaging provides an alternative way to characterize CZ structure that is cost-effective and can cover a large area. Specifically, the active source seismic refraction method has been commonly used for studies in CZ science because the acquisition geometry can be designed to achieve different spatial resolution along depth and the method is relatively easy to operate along steep hillslopes (Befus et al., 2011; Flinchum et al., 2018; Hayes et al., 2019; Holbrook et al., 2014; St. Clair et al., 2015). Seismic refraction imaging is done by identifying the *P*-wave arrival time at each seismic receiver (geophone) from an artificially generated

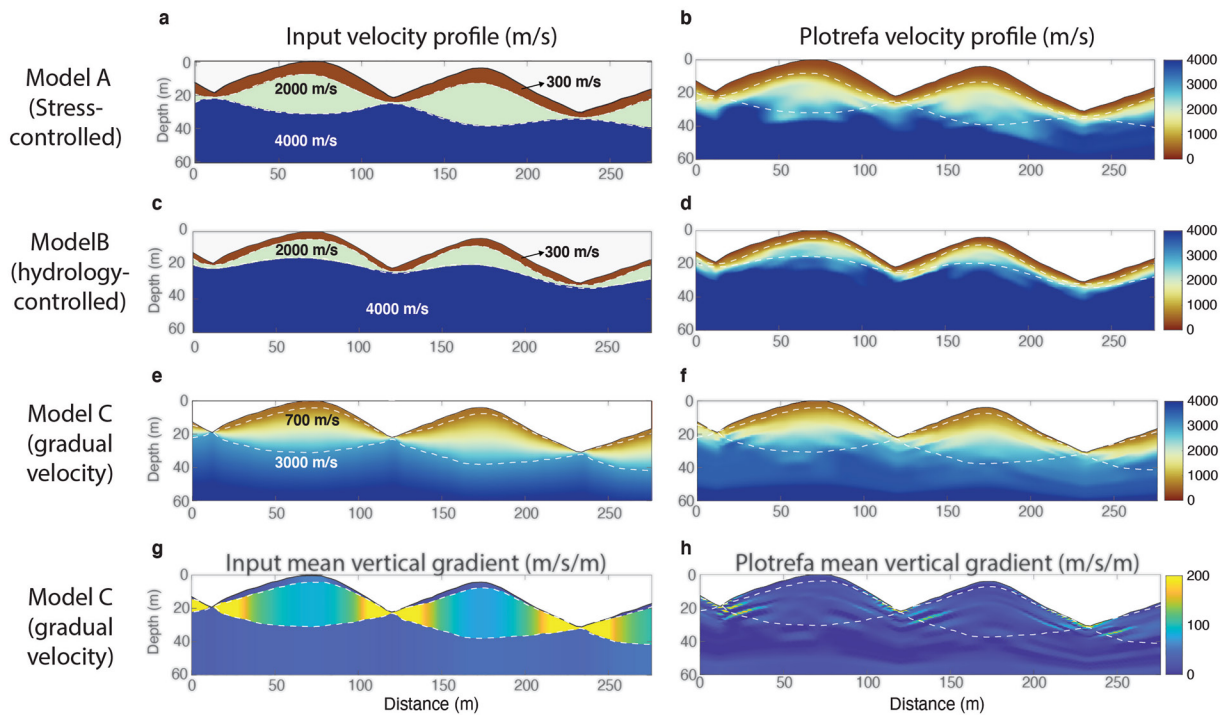


**Figure 1.** Schematic models of three hypotheses for subsurface CZ structure. (a) Stress model (model A), where the CZ structure is mainly influenced by regional stress fields. (c) Hydrology model (model B), where the CZ structure is regulated by channel incision. (e) Combined gradual model (model C), where a shallower change in velocity gradient is subparallel to the surface, and a deeper gradient change mirrors topography, amidst gradually increasing seismic velocity with depth. (b, d, and f) show the predicted CZ structures using seismic refraction with the commercial software *Plotrefa*. (g and h) show the mean vertical gradient for model C generated from the input and using *Plotrefa*. Without an uncertainty estimate of the mean velocity, there is no rigorous way to fully resolve the lower boundary of the model. CZ, critical zone.

seismic source (Julian & Gubbins, 1977). In principle, greater depths can be investigated by increasing the distance between source and receiver (i.e., the off-end shot distance) and shorter receiver intervals can resolve shallower velocity structure. Because seismic velocity is affected by rock type and the degree of weathering, constraints on subsurface seismic velocity from *P*-wave arrival data can be used to infer material type, fracture density, and water content (Holbrook et al., 2014).

Commercial software packages such as *Plotrefa* developed by Geometrics (<http://www.geometrics.com>) and *DW Tomo* by Geogiga (<http://geogiga.com>) are commonly used in seismic refraction for CZ studies (e.g., Befus et al., 2011; Holbrook et al., 2014; Pasquet et al., 2016; St. Clair et al., 2015). These approaches start from an initial velocity structure and iteratively perform the inversions until the model misfit to the arrival time reaches a certain threshold value. Iteration is necessary because of nonlinearity inherent in the inverse problem: the unknown velocity structure determines the paths taken by the seismic waves, which, in turn, defines how sensitive individual recorded travel-times are to the velocity structure itself. The inversions are regularized by parameters defining model resolution and smoothing, which are set by the user at the start of the inversion. For example, St. Clair et al. (2015) impose model smoothing to prevent overfitting and reduce the number of model parameters. They also repeat the inversions with many different initial models to ensure that the final velocity model is not influenced by the initial model. However, these classical approaches do not extensively explore the uncertainty and tradeoffs in the inverted velocity models, nor do they assess the effect of horizontal and vertical model smoothing assumptions. These limitations hinder interpretation, particularly of deeper structures. For example, seismic velocity models in Figures 1b, 1d, and 1f are inverted by using *Plotrefa* with synthetic data calculated from Figures 1a, 1c, and 1e with imposed Gaussian noise (detail described in Section 3.2). Solely based on the inverted results without the knowledge of data uncertainty, we cannot rigorously assess model resolution at greater depth and therefore distinguish the CZ models. Indeed, quantifying uncertainty and influence of prior assumptions is indispensable when testing hypotheses regarding CZ structure.

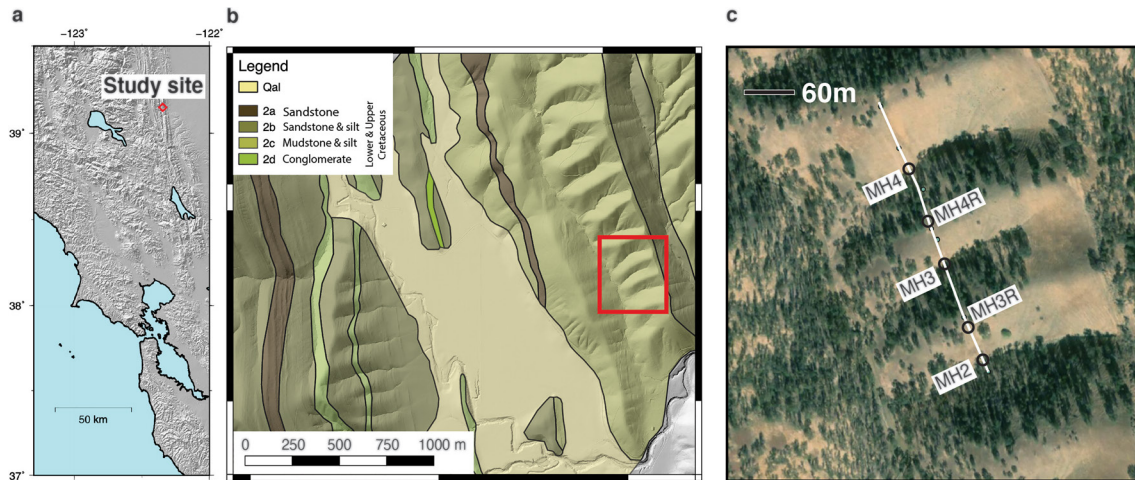


**Figure 2.** Field site location. (a) Study site (Rancho Venada) location in Northern California. (b) Regional geology with hillshade background. The lower- to upper-Cretaceous sedimentary Great Valley Sequence rocks dominate this region. The red square indicates the study site in (c). (c) Location of the shallow seismic refraction transect (Figures 7 and 8). The background optical satellite image downloaded from Google Earth shows clear contrast between vegetated north-facing slopes and unvegetated south-facing slopes. MH2, MH3, and MH4 represent the dry channels that run across the survey line, and MH3R and MH4R are the ridgetops along the survey line (also labeled in Figure 8).

In this study, we tackle a few aspects of CZ research using seismic refraction methods. We develop a seismic velocity inversion strategy for near-surface geophysics that does not require regularization parameters such as model smoothing or damping, and more fully quantifies uncertainty of the velocity models. The strategy is based on self-parameterizing (i.e., transdimensional), probabilistic (i.e., Bayesian) inversion of travel-time measurements, where the measurement uncertainty is also estimated in the inversion (i.e., hierarchical). To explore the capability of this Transdimensional, Hierarchical, Bayesian (THB) approach to distinguish different velocity structures, we design three 2D candidate models, predict traveltimes through them for various acquisition geometries, and invert these predicted traveltimes using our THB approach. We quantitatively assess the accuracy of retrieval for each velocity structure, as well as the model uncertainty at depth. Finally, we conduct field surveys along hillslopes in the Cretaceous sedimentary Great Valley Sequence in California (Figure 2) and invert traveltimes from the surveys using the THB approach in order to characterize the CZ structure of the study site.

## 2. THB Approach

In this section, we describe our approach for inverting shallow seismic refraction data to produce estimates of subsurface seismic velocities. Traditional inversions obtain a velocity model that most closely predicts measurements and may introduce spurious structures when attempting to fit measurement noise or errors introduced by modeling approximations. Typically, only a single model is obtained, and uncertainty quantification is limited and often neglects any nonlinearities inherent in the inversion (e.g., Tarantola & Valette, 1982). Because inversions for velocity structure are usually a mixed-determined problem, prior information about the model must be introduced. This is commonly done by imposing smoothing or damping (Menke, 1984), though formulations in terms of a priori distributions on the model parameters are also common (Tarantola & Valette, 1982). Measurement and modeling noise, such as that due to picking uncertainty and the approximation to actual 3D seismic raypaths, are poorly known in active source seismic surveys. Thus, the reliability of model characteristics is difficult to estimate, complicating hypothesis testing and interpretation.

The THB inversion scheme attempts to alleviate some of the limitations of traditional inversion approaches in two ways: (1) It treats model complexity (i.e., the number of unknowns) as an unknown to be estimated from the data (Malinverno, 2002; Sambridge et al., 2006); (2) It estimates measurement and modeling error explicitly through the inversion (Malinverno & Briggs, 2004). Here, we implement THB inversion using the reversible jump Markov chain Monte Carlo (rjMCMC) algorithm (Green, 1995) and obtain an ensemble of

velocity models. A posteriori probability density of parameters of interest (such as velocity at a location, number of velocity layers, data measurement uncertainty, etc.) can be estimated from the ensemble, allowing uncertainties and tradeoffs to be quantified. Crucially, the inversion scheme exploits the nonuniqueness inherent in seismic inversions, which exhibit as multimodal posterior distributions, particularly near structural boundaries (e.g., Burdick et al., 2019; Galetti et al., 2015; Olugboji et al., 2017).

Transdimensional approaches to traveltimes tomography in 2D (Bodin & Sambridge, 2009) were extended to explicitly estimate data error through hierarchical parameters (Bodin et al., 2012) and to 3D tomography on local (Piana Agostinetti et al., 2015) and continental (Burdick & Lekic, 2017) scales. THB approaches have been applied to the inversion of controlled-source data in 2D dimensions: geoacoustic imaging (Dettmer & Dosso, 2013), full waveform reflection inversion (Ray et al., 2018; Visser et al., 2019), marine electro-magnetic sounding (Ray & Myer, 2019; Ray et al., 2014), electrical resistivity imaging (Galetti & Curtis, 2018), and refraction traveltimes tomography (Ryberg & Haberland, 2018).

Here we follow the approach of Ryberg and Haberland (2018), and only briefly describe the concept and the process for near-surface applications. A user guide of this program can be found in Supplementary Material. In this inversion scheme, the user proposes an initial velocity model and priors of model parameters, including the lower and upper bounds of each model parameter (e.g., computational grid resolution, velocity range, number of control points, noise parameter, total iterations). The data uncertainty term includes both the measurement errors associated with *P*-wave arrival time picking and errors introduced by approximations in forward-modeling, such as the treatment of 3D sensitivity of traveltimes to velocity variations. This uncertainty term is usually not quantified but it impacts the complexity of the models retrieved through inversion. The prior for this uncertainty term is assumed to be a uniform distribution with user-set minimum and maximum limits, and the posterior distribution is estimated through the THB inversion. This estimated uncertainty term is referred to as the “noise hyperparameter” and can provide an objective estimate of data uncertainty (Bodin et al., 2012).

For the velocity structure, an initial velocity model is constructed by a number of control points, each of which has a velocity associated with it. The velocity at arbitrary locations in the model domain is given by Delaunay piecewise-linear interpolation of the control point velocities (Figure 3a) (implemented using *scatteredInterpolant* function in Matlab), and the number of control points can increase or decrease during the rjMCMC iterations. Similar approaches have previously been implemented in Ryberg and Haberland (2018) and Hawkins et al. (2019). There are several methods to interpolate the velocity of control points. As tested by Ryberg and Haberland (2018), interpolation using Delaunay triangulation (Figure 3c) can produce smaller velocity jumps and therefore more realistic earth structure than using Voronoi cells with constant velocity within a cell (Figure 3b). For the length scales relevant to CZ science (meters to submeters), the transitions from soil, saprolite, to bedrock are normally gradual. We therefore use Delaunay piecewise-linear interpolation. Additionally, like Voronoi cells, the Delaunay triangles can conform to arbitrary geometries, making this parameterization suitable for reproducing more than just simple layered structures. To start, we set the control points at the four corners of the model domain fixed with at least one free control point within the model domain. The maximum number of control points is set by the user, and the location of each control point is varied during iterations, along with its associated velocity.

The user inputs the locations of the sources and receivers on the model domain, which are on the ground surface in this study. Since obtaining meaningful estimates of the posterior distribution requires computing travel-times through velocity models proposed during large numbers ( $\sim 10^5$ – $10^7$ ) of rjMCMC steps, computational efficiency is crucial for ensuring practicability. To that end, we use the Fast Marching Method to expedite calculations (Rawlinson & Sambridge, 2005; Sethian, 1996), specifically the Matlab Fast Marching Method (FMM) toolbox (Kroon, 2021; Peyre, 2020; Peyre & Cohen, 2004) to compute *P*-wave arrival time at each receiver from the source.

The posterior probability of a set of model parameters  $\{m_j\}$  given the set of measured traveltimes data  $\{d_i\}$ ,  $P(\{m_j\} | \{d_i\}, I)$  is given by Bayes' Theorem ( $\{ \}$  indicates a collection of values):

$$P(\{m_j\} | \{d_i\}, I) \propto P(\{d_i\} | \{m_j\}, I) P(\{m_j\} | I), \quad (1)$$



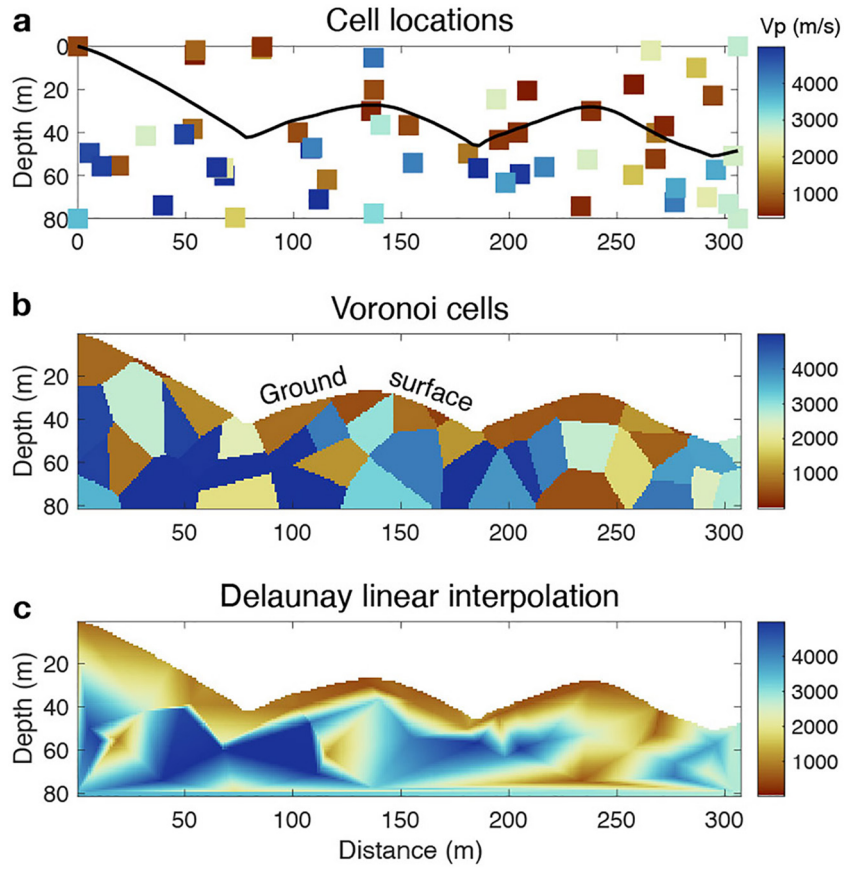


**Figure 3.** Schematic model geometry and interpolation of THB2D. (a) Location of cells in the model domain. The color of the cells represents seismic velocity. The black line is the surface topography. (b) Velocity interpolation using Voronoi cells. (c) Velocity using Delaunay linear interpolation.

where  $I$  is the relevant background information, including grid spacing that can capture the size of structure of interest, etc.  $P(\{m_j\} | I)$  is the prior probability distribution on the model parameters, which can be defined by the users based on the knowledge of the region targeted in the inversion (e.g., range of seismic velocity, number of control points in horizontal and vertical, etc.).  $P(d_i | \{m_j\}, I)$  is the likelihood function that depends on the goodness-of-fit between predicted and measured  $P$ -wave arrival times:

$$P(d_i | \{m_j\}, I) = (2\pi)^{\frac{-N}{2}} \prod_{i=1}^N \sigma_i^{-1} \exp \left( -\sum_{i=1}^N \frac{(T_i - T_i^{\text{obs}})^2}{2\sigma^2} \right), \quad (2)$$

where  $T_i$  and  $T_i^{\text{obs}}$  are the travel times predicted by the proposed model and observed arrival times, respectively.  $\sigma^2$  is the variance of data error related to picking uncertainty and other error sources, which is parameterized by the noise hyperparameter. In this study, we assume that data error does not change with source-receiver distance, and that the noise is not spatially correlated. In Text S5, we show how error that increases with source-receiver distance affects the inversion results. Implementation of spatially correlated data noise and the design of the hyperparameters is described by Dettmer et al. (2012).

The basic concept of Markov Chain is that a new model is proposed by changing one parameter from the previous model, and whether or not the proposed model is accepted or rejected depends on the change in posterior probability following the Metropolis-Hastings condition (Metropolis et al., 1953). In rjMCMC,

proposed models can have higher or lower dimensionality (the number of model parameters, i.e., control points, is not fixed). There are three major stages as follows.

- (1) Propose a new model through a random walk process:

At each iteration, a new model is proposed by changing the current model. This is done by randomly selecting one of six operations: (1) change velocity of a control point, (2) add a control point, (3) remove a control point, (4) move a control point, (5) exchange velocity between two random control points, and (6) change the noise hyperparameter. Random changes to the velocity, noise hyperparameter, and control point locations are drawn from normal proposal distributions defined by the user (see Text S3 for more detail). Velocities for added control points are drawn at random from the uniform distribution of the velocity prior.

- (2) Compute travel time using FMM:

Compute travel-time based on the new proposed velocity model using the Fast-marching method (Peyre, 2020), and compare with the observed travel-times.

- (3) Randomly accept or reject the proposed model:

Proposed models are accepted or rejected according to an acceptance probability that includes both the prior and the fit to the data (see Metropolis et al., 1953; also see Text S3). When the proposed model is rejected, the current model remains for the next iteration. When the proposed model is accepted, the proposed model replaces the current model for the next iteration.

At the start, during the so-called “burn-in” period, the rjMCMC proposes velocity models that still bear the signature of the starting model and have relatively high misfit. After a sufficient number of iterations, misfit starts to stabilize at a relatively low value and the velocity models no longer depend on the starting model. Models are not saved to the ensemble until after this burn-in period ends. Since models proposed at a given rjMCMC step are correlated to those from the previous step, we wait 200 steps between saves to the ensemble (this “thinning” interval can be defined by the user). We summarize the velocity structures in the ensemble by their mean and represent uncertainty by computing the variances of the model parameters. Parameter tradeoffs can be summarized by the covariances computed from the ensemble. Uncertainty of the modeled velocity inversion is central to interpreting “real” versus “artificial” subsurface features.

### 3. Synthetic Tests

When conducting shallow seismic surveys in the field, one chooses the spacing of geophone receivers and off-end shots. The choice of this spacing (e.g., 3 m between geophones) controls the shallowest resolution of the survey. To determine the field configuration that can best resolve CZ structure with practical limitations, we first use THB traveltimes inversion to explore several 1D synthetic tests with different levels of measurement uncertainty and off-end shot distance, as described in Text S1. Following this, we perform 2D synthetic tests to investigate the resolving power at depth in different CZ structures. Finally, we compare performance in model robustness between the THB approach and commercial software.

#### 3.1. 2D Synthetic Test of Layered Structures

The goal of the 2D synthetic test is to investigate whether the field configuration suggested from the 1D test (see Text S1) can be used to distinguish different 2D velocity structures (Figures 1a, 1c, and 1e). We also want to test how seismic velocity distributions are resolved between commercial software and the THB approach. We create the synthetic CZ structures based on two end-member CZ models: (1) CZ lower boundary topography mirrors surface topography from channels to ridgetops (stress-controlled model, or model A; Figure 1a) (St. Clair et al., 2015), (2) CZ lower boundary topography increases upslope from channels to ridgetops (hydrology-controlled model, or model B; Figure 1c) (Rempe & Dietrich, 2015), and (3) a 2D structure with gradual increase of velocity in each layer, or model C (Figure 1e).

For the first two tests, we set up a three-layer model, with a top layer ( $V_p = 300$  m/s) that is 4–8 m thick to represent a soil layer, a middle layer ( $V_p = 2,000$  m/s) as the weathered bedrock layer, and a bottom layer ( $V_p = 4,000$  m/s) as the fresh bedrock layer (Figures 1a and 1b). For the third synthetic test, we set the

velocity to gradually increase in each layer (Figure 1e). In this design, we set a shallower layer boundary that is subparallel to the ground surface, and a deeper layer boundary that is similar to the lower boundary of the stress model (Figure 1a). At shallower depth ( $< 4$  m), the velocity of the top layer increases from 450 to 700 m/s. This top layer is not present at the channels. For the middle layer, the velocity increases from 700 to 3,000 m/s and the maximum layer depth is between 30 and 40 m. For the bottom layer, the velocity increases from 3,000 to 5,000 m/s at the bottom of the model domain.

We set up the synthetic seismic survey similar to the actual field survey, assuming 24 geophones at 3 m intervals. This means that we survey the entire synthetic landscape 69 m at a time. The maximum off-end shot distance is 36 m, and shots are made every 9 m until 36 m past the last geophone. We then move this survey to the next 69 m along the hillslope until completion of the entire transect. Since the maximum off-end shot is 36 m away from the first/last geophone, the first and last geophones are placed 36 m from the end-boundary of the model domain (Figure 1a). We estimate the *P*-wave arrival times from a shot to every geophone using the FMM (Peyre, 2020; Rawlinson & Sambridge, 2005; Sethian, 1996). To simulate possible human *P*-wave picking errors or other sources of noise, we add Gaussian noise with a standard deviation (one-sigma) of 2 ms to all *P*-wave arrival times for models A and B, and 1 ms Gaussian noise to model C. The Gaussian noise level is the same in all source-receiver distances. In practice, the data uncertainty due to picking error could increase with source-receiver distance. In Text S5, we show a synthetic test in which data error increases with distance. We test the synthetic data by running the commercial software *Plotrefa* and the THB inversion.

### 3.2. Plotrefa

We first use *Plotrefa*, a commercial software developed by Geometrics Inc. for inverting velocity models of the synthetic tests. We set the model mesh size as 3 m horizontally and between 1 and 4 m vertically with layer thickness increasing with depth (Figure S3). Although *Plotrefa* may achieve better performance with finer model mesh size, we are not able to generate high resolution models because of the restrictions of our license. The modeled seismic velocity can be varied between 250 and 5,000 m/s. *Plotrefa* sets up an initial velocity structure with the lowest velocity (250 m/s) near the ground surface to the highest velocity (5,000 m/s) at the bottom of the model, which is a total of 70 m below the highest ground surface elevation.

For models A, B, and C, we continue the inversions until the predicted velocity structures do not vary significantly after multiple iterations. The final predicted velocity models are shown in Figures 4a, 4b, and 5a. The dashed contour lines in Figures 4a, 4b, and 5a are the layer boundaries between the top and middle and the middle and bottom layers in the input models (Figures 1a, 1c, and 1e). The vertical velocity gradient plots (Figures 4c, 4d, and 5b) represent the depth where seismic velocity increases more rapidly and can be a good indicator of where material boundaries are.

In general, the true layer boundaries are roughly located where there is a change of color (i.e., seismic velocity). The result seems to fit model B better (Figure 4b); however, as the model mesh structure at shallow depth is parallel to the ground surface (Figure S3), the velocity model result may preferentially favor velocity boundary structures that are similar to the ground surface (e.g., model B). An alternative way to identify velocity layers is using the vertical velocity gradient. For models A and B, as the seismic velocity changes abruptly between velocity layers in the input synthetic structures (Figures 1a and 1c), the vertical velocity gradient should increase near the boundaries of these layers. However, in the vertical velocity gradient of the velocity models (Figures 4c and 4d), we are unable to clearly identify velocity layers due to blurred and discontinuous colors. For model C, although the velocity model (Figure 1f) reproduces the gradual velocity increase with depth of the input model (Figure 1e), the change of velocity gradient with depth in the input (Figure 1g) is not predicted by the model (Figure 1h). Due to the model mesh structure (Figure S3), most of the high velocity gradients occur along meshing rather than along true velocity boundaries. As uncertainty estimates are not provided with *Plotrefa* (or traditional inversion methods), we are unable to determine whether or not the complexity between the mid- and high-velocity layers shows the real topography of the velocity boundary, or is due to the mesh structure and/or over-fitting measurement noise. Without this knowledge, we are unable to properly image this boundary or to rigorously distinguish the bottom layer topography between models A and B.

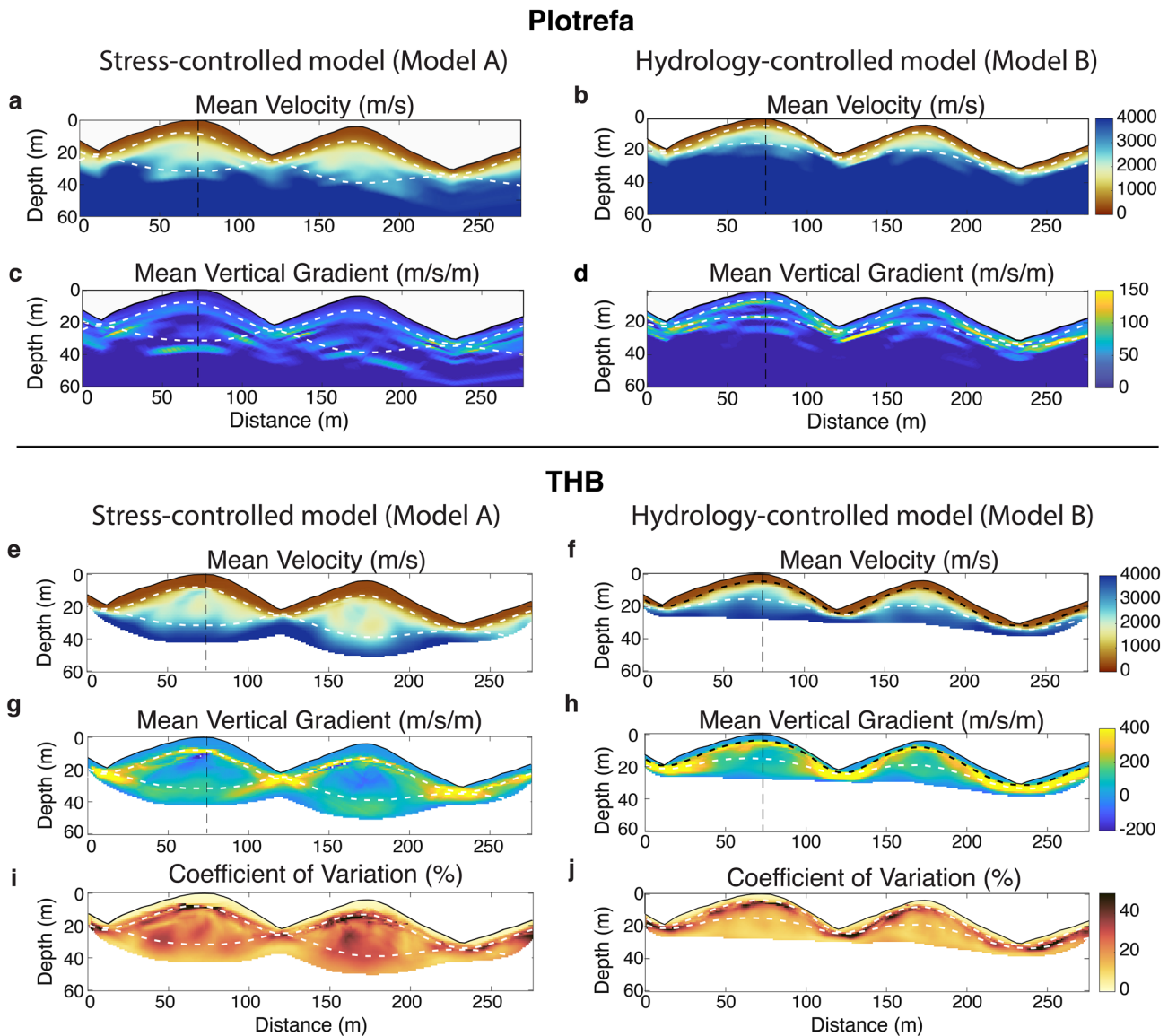


**Figure 4.** 2D synthetic tests of models A and B using *Plotrefa* and THB. The input velocity models are from Figures 1a and 1c. Subplots (a–d) are the results from *Plotrefa*, and (e–j) are the results from THB. The black or white dashed lines in each subplot are the layer boundaries between the top, middle, and bottom layers shown in Figures 1a and 1c. The vertical dashed lines in the subplots show the locations of the vertical velocity profiles in Figure 6. THB, Transdimensional Hierarchical Bayesian.

### 3.3. THB Method

For all models, we set the model thickness as 60 m with 1 m horizontal and vertical grid spacing. We perform  $2 \times 10^6$  iterations with 10 Markov Chains. This amount of iterations, Markov Chains, and model size took about 80 h of computation time for all models in a workstation with an 18-core Intel Xeon Gold 6140 processor.

For models A and B, the RMSE misfit evolutions (Figures S4a and S4c) show that the misfits start to stabilize at a constant level after  $\sim 3 \times 10^5$  iterations. We set the “burn-in” conservatively at  $1 \times 10^6$  iterations. In the model misfit and uncertainty analyses (Figures S4b and S4d), the noise hyperparameter that can be considered as data measurement uncertainty is  $\sim 2.3$  ms for both models. The RMSE misfit is  $\sim 2.3$  ms for both models A and B. The RMSE misfit and the noise hyperparameter values are roughly the same, indicating that THB can fit the data with the same level of misfit as the noise hyperparameter (i.e.,  $\chi^2 \approx 1$ ). However,



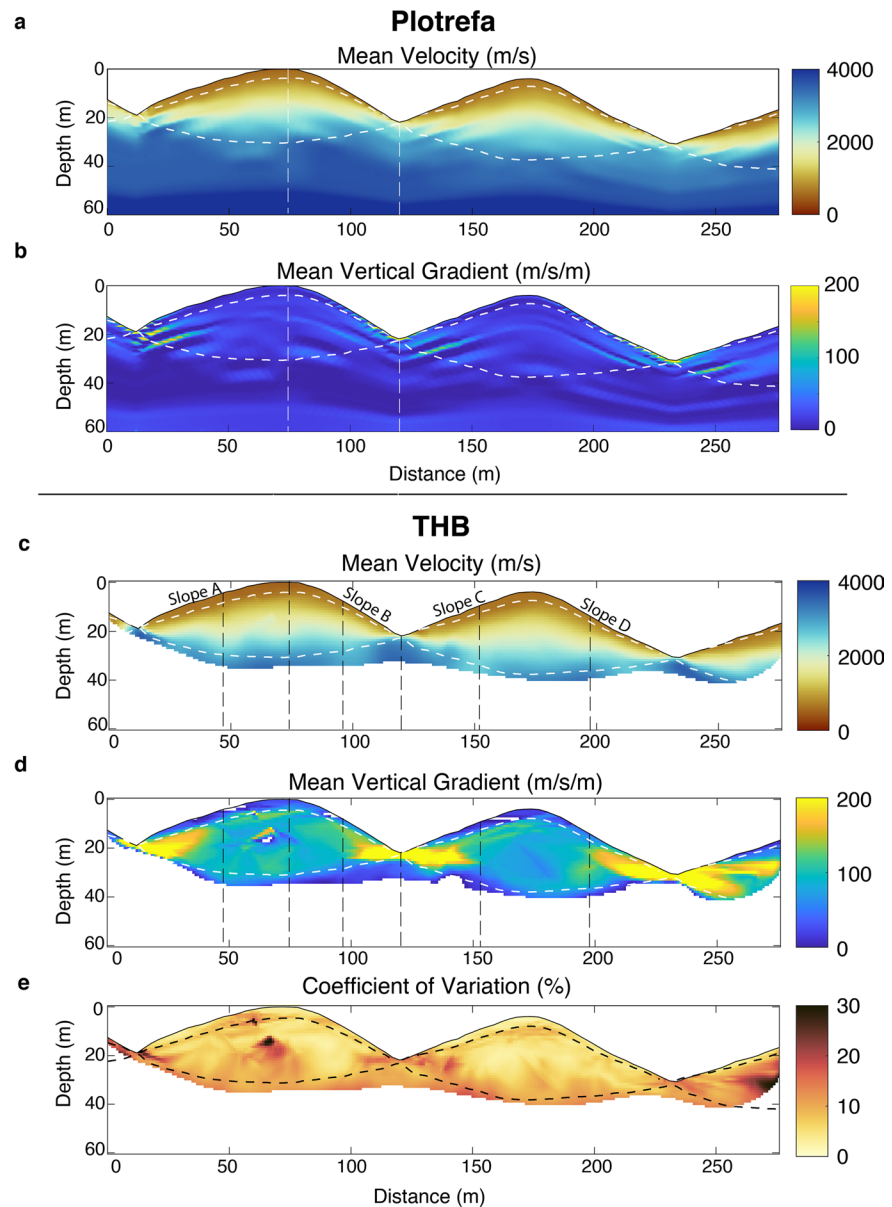


**Figure 5.** 2D synthetic test of model C using *Plotrefa* and THB. The input velocity model is from Figures 1e and 1g. (a and b) are the results from *Plotrefa*, and (c–e) are the results from THB. The black or white dashed lines in each subplot indicate the highest change in gradient, separating the top, middle, and bottom layers shown in Figure 1e. The vertical dashed lines in the subplots show the locations of the 1D velocity profiles in Figure 6. THB, Transdimensional Hierarchical Bayesian.

we note that the hyperparameter is about 15% greater than the imposed Gaussian noise (2 ms). This deviation is likely due to the implementation of sharp velocity boundaries that cannot be properly modeled with Delaunay interpolation (Figure 3c). The mean velocity model in the ensemble obtained by THB has a mean misfit of  $\sim 1.9$  ms, which is close to our imposed Gaussian noise. In comparing the mean misfit versus source-receiver distances of both models (Figures S4b and S4e), there seems to be a higher misfit level in shorter source-receiver distances, even though the level of imposed Gaussian noise is the same in all source-receiver distances.

The mean velocity, vertical velocity gradient, and model uncertainty (illustrated by the coefficient of variation, which is standard deviation divided by the mean of the posterior distribution) of the ensemble of

models obtained by THB for scenarios A and B are shown in Figures 4e–4j, and other related plots are in Figure S4. For both input models A and B (Figures 1a and 1c), THB predicts roughly three velocity layers, with (a) a top layer < 500 m/s near the ground surface, (b) a ~2,000–3,000 m/s middle layer, and (c) a ~4,500 m/s bottom layer (Figures 4e and 4f). Model A detects a more irregular middle layer, with a rapid increase and then decrease in velocity below both ridgetops. The transition between layers can be highlighted by plotting the vertical velocity gradient (Figures 4g and 4h), as the seismic velocity increases more rapidly near layer interfaces. Between the top and middle layers, the velocity gradient is > 400 m/s/m, indicating a sharper velocity increase. The location of the inferred interface fits remarkably well with the input velocity boundary (black and white dashed contour lines in Figure 4). The boundary between the middle and bottom layers is also shown by the increase of velocity gradient to ~200 m/s/m (Figures 4g and 4h), but is less pronounced in model B. The coefficient of variation of the posterior ensemble represents the model uncertainty, and is < 5% for the top layer of both posterior models (Figures 4i and 4j), with a much higher variation (50%) along the transition from the top to the middle layer. The uncertainty of the middle layer ranges from 15%–35% in model A and 10%–15% in model B. The bottom layer has a 10%–20% and 10%–15% uncertainty for models A and B, respectively. Lower coefficient of variation values does not necessarily indicate more accurate fitting of the input, but rather greater consistency between models in the accepted ensemble. In fact, model B has a lower coefficient of variation than model A and yet model A achieves a better fit to the input. Nevertheless, higher uncertainty values can tell us about the resolution power of our setup and may be useful in interpreting the predicted model. For example, the regions of high variation along the layer transitions arise due to uncertainty of where the exact layer transition occurs, and can be used to map out interfaces (e.g., Burdick & Lekic, 2017; Olugboji et al., 2017). The smoothness of the layer transition in the mean model is not inherently due to smoothness in the target velocity gradient, but can be due to an averaging over different locations in iterations (e.g., Burdick et al., 2019).

For the combined model (model C), after  $2 \times 10^6$  iterations, 10 Markov chains converge to a mean misfit of ~0.9 ms with burn-in set as  $1 \times 10^6$ . Due to lower input noise, model C has a lower mean misfit than models A and B. The hyperparameter is 1.07 ms, which is very close to the imposed Gaussian noise (1 ms). This result indicates that the Delaunay interpolation can properly infer data noise when the layer boundaries are not sharp. The results for model C are shown in Figures 5c–5e and Figure S4. The mean velocity profile predicts layers within which velocity increases gradually, and captures the thickening of the top layer (< 700 m/s) toward ridgetops. The mean vertical gradient is able to detect the two changes in gradient described in the input setup: one subparallel to topography, and the other mirroring topography. Both interfaces have a mean vertical gradient of 100–125 m/s/m. Both the shallower and deeper interfaces are gradual transitions, but can still be detected by THB rjMCMC. Uncertainty is 5%–10% throughout much of model C (Figure 5e). There is a slightly higher uncertainty closer to the channels and toward the bottom of the profile. The far-right and far-left edges of the model have uncertainty > 15% likely due to fewer ray paths constraining that section. There is likewise a region of high uncertainty (30%) below the first ridgetop where velocity decreases.

The input velocity for model C was designed with a thicker top layer on north-facing than on south-facing hillslopes. As the model grid size is set to 1 and 3 m for geophone intervals, this level of grid resolution cannot well resolve the thickness variation. The 2-m variation in thickness is recovered to an extent by THB, with vertical velocity and vertical gradient profiles from slope A and slope C distinguishably different from slope B and slope D in the first 4 m (Figure 6e). Changes in velocity gradient for south-facing and north-facing slopes occur at roughly 2 and 4 m depths, respectively, corresponding to the input model. However, differences between the model profiles become more muddled at depth. From this test, we see that THB can capture gradual increases in velocity and changes in velocity gradient with the presence of measurement noise, though it may produce a broader zone of transition than actually exists.

To explore whether the initial velocity model could influence the posterior mean velocity distribution, we also perform THB inversion for model C with two different initial velocity distributions: (1) constant initial velocity of 2,000 m/s and (2) initial velocity increasing with depth. As demonstrated in Figure S4, given a sufficient number of iterations, the posterior mean velocity model should be independent of the initial velocity distribution. We additionally show the mean velocity model during the intermediate period (before burn-in) to show the evolution of the velocity distribution from the initial model to after burn-in.

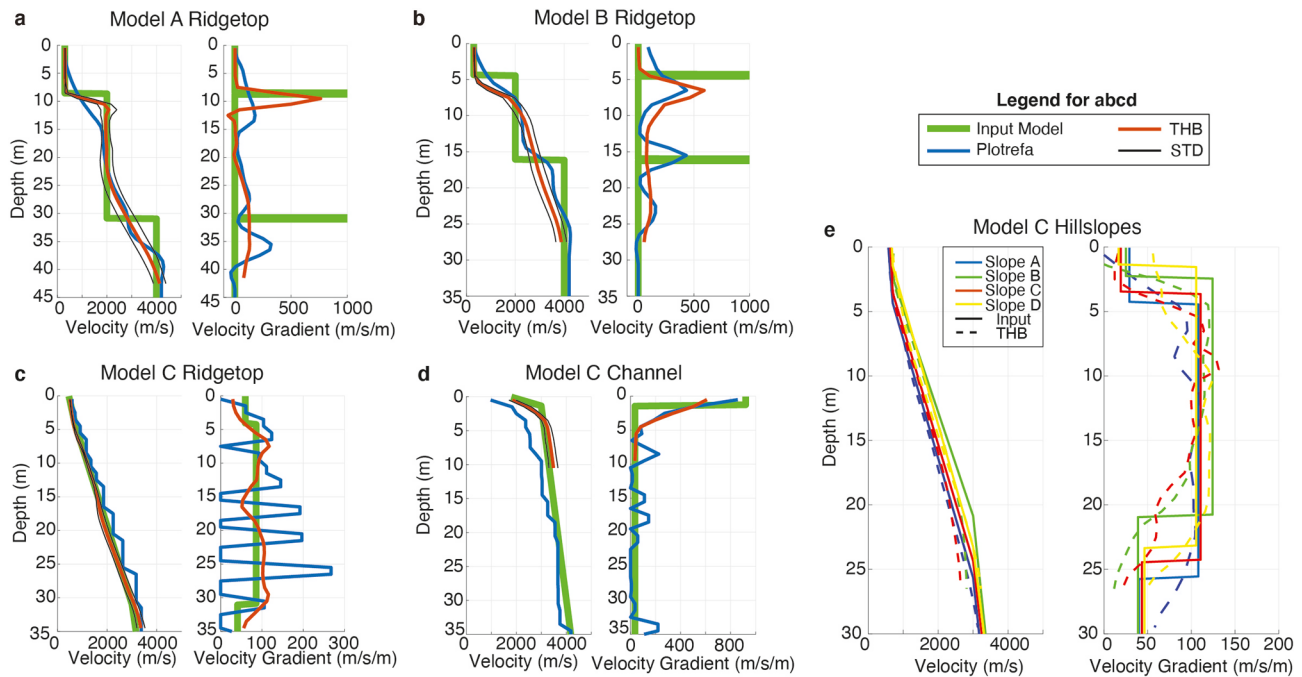


**Figure 6.** Vertical velocity and velocity gradient profiles of the 2D synthetic tests. The profiles are below the highest elevation of the models (vertical dashed lines in Figure 5). (a–c) are the vertical profiles below ridgetops for models A, B, and C, respectively. (d) is the vertical profile below the channel for model C. The green lines are the input velocity structures. The blue and orange colors represent the inferred velocity structure using *Plotrefa* and THB, respectively. The black lines are the 1-sigma confidence interval of the THB model. (e) shows vertical profiles below north- (blue and red lines) and south-facing (green and yellow lines) hillslopes of model C. Solid lines are the input velocity and dashed lines represent inferred velocity structure using THB. THB, Transdimensional Hierarchical Bayesian.

### 3.4. Comparison of Traditional Inversion and the THB Approach

In the 2D synthetic tests, *Plotrefa* is able to resolve increases of seismic velocity at depth with roughly correct velocities at shallower (< 10 m) depth (Figure 1). However, for depths greater than 20 m where velocity is greater than 2,000 m/s, *Plotrefa* is not able to clearly recover the deep structure of the three synthetic velocity structures (Figures 4a, 4b, and 5a). In model A, *Plotrefa* captures increased CZ thickness, but the shape of the bottom layer boundary is more irregular and therefore it is hard to confidently resolve the topography of the bottom layer (Figure 4a). Additionally, the inferred velocity structure can be significantly influenced by the model meshing structure, as the meshes are subparallel to the surface topography (Figure S3). On the other hand, the THB approach is able to clearly differentiate the synthetic velocity structures (Figure 4e). At shallower depths, both *Plotrefa* and THB can resolve the top layer equally well, but THB predicts a much sharper boundary between the top and middle layers.

To better compare results between *Plotrefa* and THB, we plot the vertical velocity and vertical velocity gradient below the tallest ridge (labeled by the vertical black dashed line in Figures 4a and 4e). As shown in Figure 6a, for Model A we find a much better agreement between the input velocity structure (green line) and the inferred structure by THB (orange line with black standard deviation) than the velocity profile predicted by *Plotrefa* (blue color). THB predicts one high gradient peak, and a second more gradual increase in velocity, implying two layer boundaries in the inferred velocity structure. A sharper peak at ~9 m depth indicates a well resolved boundary, and the gentle increase to ~33 m depth has a wider distribution of the peak, implying a less well resolved boundary. The velocity gradient predicted by *Plotrefa* (blue color in Figure 6a) shows two high gradient peaks related to the layer boundaries, but the gradients are lower than those predicted by THB, and the depth of the two peaks are ~5 m below the input model. Additionally, *Plotrefa* predicts another peak at a 23–28 m depth that could be due to overfitting the imposed measurement noise. Because there is no formal uncertainty analysis in *Plotrefa*, we cannot easily determine the number of layers from the velocity gradient. As shown in Figure 4e, *Plotrefa* additionally overestimates the model A velocity at a 10–15 m depth and then predicts a velocity decrease right below. As both *Plotrefa* and

THB inversions do not impose the velocity increase with depth constraint, the velocity decrease shown in Figure 4e (also present as a negative peak in the velocity gradient in Figure 6a) is likely driven by synthetic data noise. Since *Plotrefa* imposes smoothing while THB does not, the THB mean velocity model is a more accurate reflection of the data.

In model B, although *Plotrefa* does not recover a sharp boundary between the top and middle layers, the inferred middle layer velocity is closer to the input velocity (Figures 4b and 4d). THB can predict a sharp shallow boundary with correct inferred low-velocity (300 m/s) and depth (~6 m) (Figures 4f and 4h), but the inferred mid-velocity is ~500 m/s greater than the input velocity of 2,000 m/s. Since *Plotrefa* solely minimizes model misfit without considering measurement uncertainty, it is able to identify the boundary between the middle and bottom layers. However, the shape of this boundary is more irregular (Figure 4b), and *Plotrefa* also predicts an additional layer boundary at 25 m depth, which is likely due to overfitting data noise. On the other hand, THB simultaneously minimizes model misfit and data uncertainty (i.e., noise hyperparameter), so in return it predicts a smoother boundary due to the presence of data uncertainty. The major difference between models A and B is the thickness of the middle layer (the green color layer in Figures 1a and 1c). With a thinner middle layer in model B, the crossover distance between middle and bottom layers is shorter. Combined with steep surface topographic relief, this would result in an even shorter crossover distance and therefore shorter arrival time difference between layers. When the arrival time difference between geophones is sufficiently small compared to the imposed data noise, THB may consider the true layer boundary as measurement noise. This is better shown in the vertical velocity plot in Figure 6b. Below the boundary of top and middle layers, the velocity gradient stabilizes at a near constant value below ~11 m depth. This can be an indication that THB considers the arrival time difference that determines the second layer boundary as measurement noise. With increasing number of iterations, THB rjMCMC has the tendency to further separate the middle and bottom layers. We therefore do not consider the poorer velocity model in model B as a failure for THB. It still predicts some likelihood of an appearance of a second layer with a much broader depth range, as shown in the vertical velocity gradient in Figure 6b. We also want to note that the imposed data noise in the 2D synthetic tests is higher than in the actual field survey, so THB can rigorously distinguish the stress-controlled (model A) and hydrology-controlled (model B) structures.

For model C, THB detects the sharpest change in velocity at a 6–7 m depth, and another at a 29–31 m depth below ridgetops (Figures 6c and 6d). The input velocity structure at this location indicates these changes in gradient should occur at a 4 m depth and 31 m depth, respectively. THB therefore captures a smoother version of the input gradient changes, extending the thickness over which velocity transitions occur. Vertical profiles for *Plotrefa* do capture more accurate locations below the ridgetop where the gradient changes; however, instead of producing a smooth increase in velocity with depth, *Plotrefa* detects additional changes in gradient within the middle layer where no such variation exists in the input (Figure 6c). More of these extraneous gradient peaks are seen in *Plotrefa* below the channel, while THB instead presents a well-defined velocity change that captures the transition from the middle to bottom layers. As it is not easy to compare model fitting by inspecting the mean velocity distribution (Figures 5a and 5c), we plot the residual velocity of model C, shown in Figure 7, to further gauge the accuracy of *Plotrefa* and THB. Positive residual velocities indicate model overestimation of the input velocity. While both *Plotrefa* and THB are within 300 m/s of the input velocity for much of the profile, *Plotrefa* appears to be spottier below ridgetops, with misfit regularly above 500 m/s. *Plotrefa* also underestimates the input velocity by 1,000 m/s below channels. THB is therefore more accurate at capturing the high velocity present below channels. Both have very low misfit in the low velocity layer, with slightly higher misfit where the velocity gradient changes in the input.

To summarize results from the 2D synthetic tests, the traditional inversion method such as *Plotrefa* can obtain good fits to the data, reducing nonuniqueness and model complexity through imposed model smoothing (e.g., St. Clair et al., 2015). However, it is not straightforward to choose a model smoothing value that can best account for the data uncertainty, model nonuniqueness, and the model resolution with depth. On the other hand, THB can simultaneously estimate model misfit and the noise hyperparameter, without the need for a separate model smoothing parameter. In this way, the model uncertainty (Figures 4i, 4j, and 5e) is estimated based on the ensembles of the posterior velocity distribution, which are affected by evolving estimates of measurement noise. The model inferred from this method can better represent an unbiased velocity structure due to the presence of measurement uncertainty.



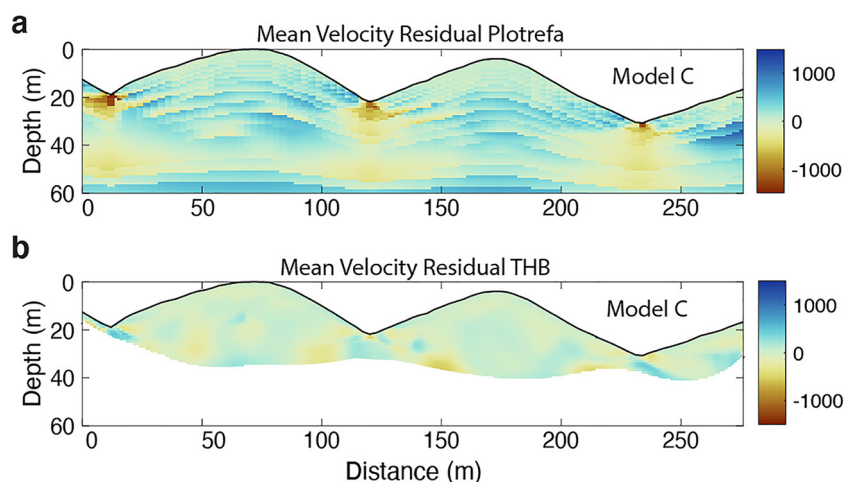


**Figure 7.** Difference between synthetic model C and the inverted models. (a) Difference in velocity between *Plotrefa* and the input. (b) Difference in velocity between THB and the input. Positive velocity residual indicates the model has overestimated the input velocity, while negative velocity indicates underestimation of the input velocity. THB, Transdimensional Hierarchical Bayesian.

## 4. Field Study

### 4.1. Study Site and Field Survey Setup

We perform an active-source shallow seismic refraction survey at Rancho Venada, near Williams, California (Figure 2a). This region has a semi-arid climate, with distinct dry and hot summers and cold and wet winters with an average precipitation of 483 mm/yr between water years 2008 and 2019 using data from the Parameter-elevation Regressions on Independent Slopes Model Climate Group at Oregon State University (<http://prism.oregonstate.edu>). Rancho Venada is located between the Northern California Coast Ranges and the Central Valley with elevation between 150 and 300 m. The Great Valley Sequence comprises regional lithology in the study site, including lower to upper Cretaceous sandstone, siltstone, shale, and conglomerate (Rich, 1971; Figure 2b). The bedrock lithology is mostly N15°W strike and ~45°–50°E dip. The strike of the sedimentary layers is aligned with the orientation of the major-ridges and trend NW-SE. In addition, the study area is dissected by low-order channels into a channel-ridge system (Figures 2b and 2c). This site is ideal for exploring CZ structure because the strike and dip of the bedrock is nearly constant, and there are no major folds or fault structures here (Rich, 1971). We design our field survey line to be parallel to the bedding strike in order to reduce complexity in subsurface bedrock structure due to lateral heterogeneity from rock type variations (Figure 2c). Therefore, the presence of lateral heterogeneity in the velocity structure could be more likely due to CZ development.

We conducted the field survey in mid-December 2019 before significant rainfall in the 2020 water year. We use the ES-3000 system with 24 14-Hz geophones manufactured by Geometrics, INC. Each 14-Hz geophone has clean-response to 240-Hz and records ground motion in a vertical component. We set the geophone (receiver) spacing as 3 m, so each survey line is 69 m (the same as geometry as in the synthetic test). The total survey line is 306 m along hillslope (273 m in horizontal distance), covering two channels and two ridgetops, with the first and last geophone located at 54 and 261 m along hillslope, respectively (46 and 232 m in horizontal distance) (Figure 2c). The black circles in Figure 8a are the location of geophones, and the mean hillslope angle is ~25° (Figure 8a). We generate the seismic source by swinging a 7 kg (12-pound) sledgehammer. For each shot location, we stack eight shots if the source is not co-located with a receiver (i.e., an off-end shot) and a stack of four shots otherwise. The farthest off-end shot is 54 m away from the first geophone. We performed a long off-end shot distance mainly because we did not know the exact CZ thickness at the site. A longer off-end shot distance also allows deeper raypaths below steep hillslopes. We set the shot interval as 9 m when the shots are within geophones, and we change the shot interval to 3 m when the shots are near ridgetops in order to better resolve shallow surface features (black cross symbols

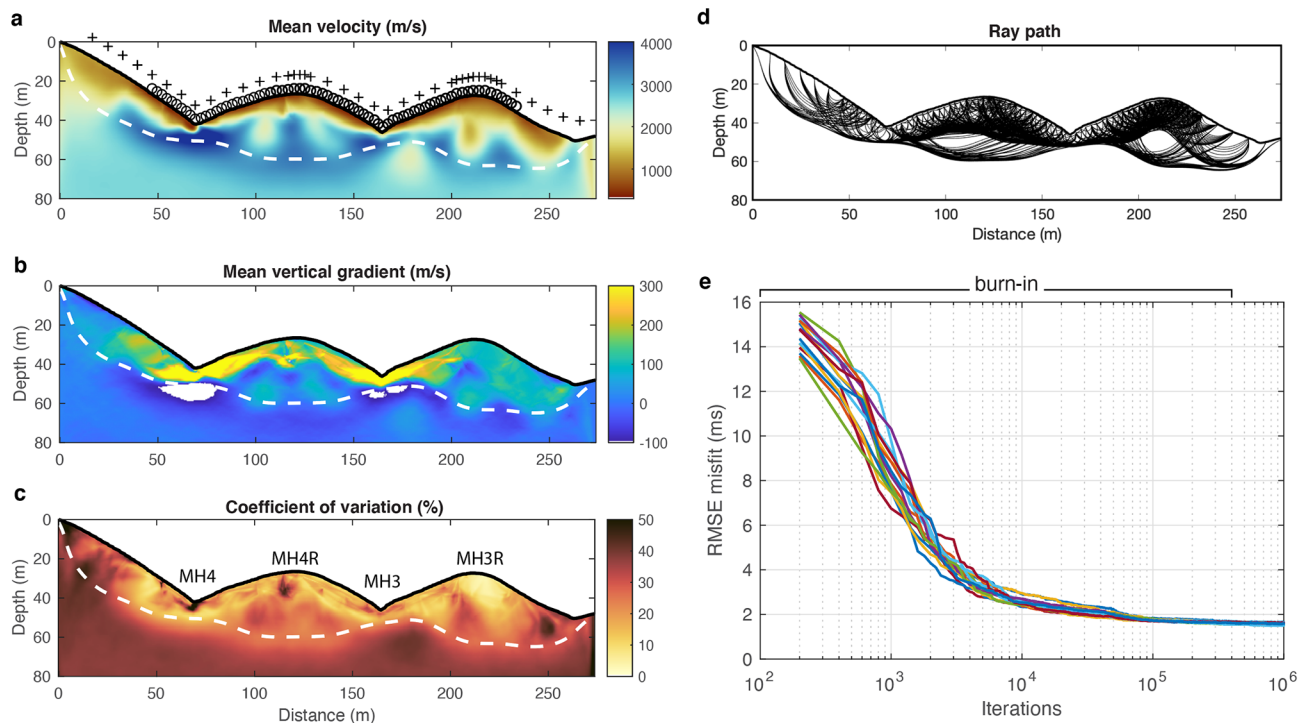


**Figure 8.** Field survey results using THB approach. (a) Mean velocity model from the posterior distribution. The black circles are geophone locations, and the black crosses are shot locations. (b) Mean vertical velocity gradient. The black circles and the black cross symbols in (a and b) are the geophone and shot locations, respectively. (c) Coefficient of variation (inferred as model uncertainty) of the posterior velocity distribution. (d) Seismic raypaths in the mean velocity structure. The white dashed line in (a–c) indicates the lowest seismic raypath. The inferred velocity below this line implies poor to no model resolution. (e) The evolution of RMS (root-mean-square) misfit of the 15 Markov Chains. THB, Transdimensional Hierarchical Bayesian.

in Figure 8a). The increased shot interval is designed to ensure sufficient raypath coverage to constrain the shallow structure near ridgetops.

The topographic profile of the field site is obtained from a digital elevation model (DEM) surveyed in an airborne LiDAR mission in 2017 (Nelson et al., 2017), and the DEM spatial resolution is 1 m. The elevation uncertainty of LiDAR DEM is normally  $<0.3$  m (Lindsay, 2006), which is much lower than the total elevation change (more than 50 m) along the elevation profiles (more than 270 m). We therefore do not consider elevation error in the survey profiles.

#### 4.2. Inferred Seismic Velocity

We pick the  $P$ -wave arrival time (i.e., traveltime) of each geophone using the software *Pickwin*, which is part of the seismic recording and processing software package by *Geometrics*. After  $P$ -wave arrival times are determined, we perform the velocity inversion using THB. The model domain is 273 m horizontally and 80 m in depth (assuming the deepest raypath could be at 80 m depth) (Figure 8a). We set the model grid resolution as 0.5 m and perform THB inversion with 15 Markov Chains with  $1 \times 10^6$  iterations for each chain. We allow velocity to vary between 300 and 5,000 m/s and set the initial number of control points to 500. The initial starting model has a gradual increase of velocity from 300 to 5,000 m/s along depth with 244 control points. As shown in Figure 8e, the misfit of early ( $<10^3$ ) iterations varies between 10 and 7 ms in the Markov Chains. After  $\sim 6 \times 10^5$  iteration, the RMSE misfit of all of the chains stabilizes to between 1.54 and 1.66 ms (Figure 8e). We therefore set the burn-in percent as 60% with a total of  $4 \times 10^5$  post burn-in iterations for each Markov chain.

The THB program shows the misfit evolution, mean velocity, vertical velocity gradient, coefficient of variation of the posterior probability, and seismic raypaths in Figure 8 (see also Figures S6 and S7 for other products). Along this transect, the coefficient of variation of the ensemble solution (Figure 8c) suggests that our

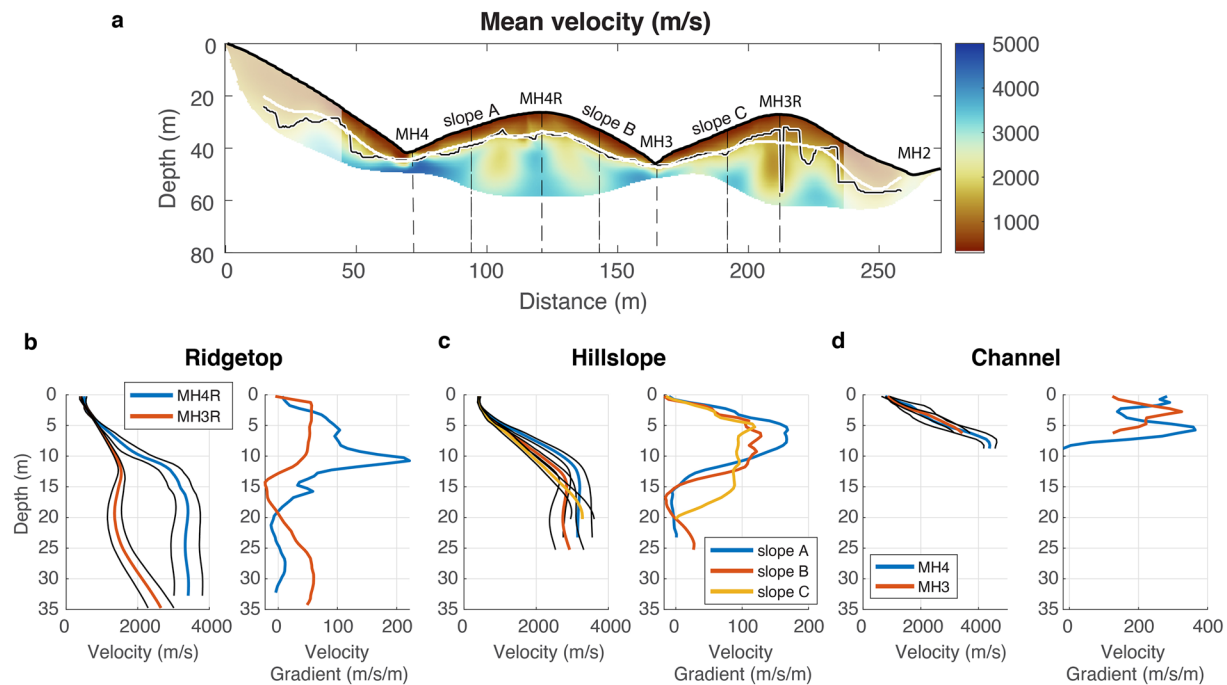


**Figure 9.** Field survey results and vertical velocity profiles. (a) Mean velocity model. The transparent edges of the profile mark areas with no geophone coverage where fewer ray paths constrain the velocity structure. The white lines are the velocity contours at 1,400 m/s. The black contour line marks the location of the highest vertical velocity gradient when seismic velocity is lower than 2,500 m/s. Note the highest vertical velocity gradient is located close to the 1,400 m/s velocity contour line. (b–d) show the selected vertical velocity and velocity gradient profiles below ridgetops (b), hillslopes (c), and channels (d). The colored curves are the mean velocity along depth, and the thin black curves are the 1-sigma confidence interval of the THB model. Note that seismic velocity increases more rapidly with depth below channels than below ridgetops. THB, Transdimensional Hierarchical Bayesian.

field survey configuration can resolve velocity structure to ~10–30 m below surface, with deeper imaging resolution below hillslopes and ridgetops. The variation of resolved depth range is due to surface topography and the actual velocity at depth. As demonstrated in 2D synthetic tests, the resolving depth would be deeper in the presence of a thicker layer of low-velocity material (Figure 4e). In the mean velocity distribution, the depth of low to high velocity transition is generally shallower below valley bottoms than ridge tops. This pattern is clearly shown in the vertical gradient (Figure 8b), where high gradient values represent a sudden increase in seismic velocity. The vertical gradient plot suggests that there is at least one steep velocity increase from ~900 to ~3,000 m/s near ridgetops and from ~1,200 to ~4,000 m/s below channels.

In comparison of misfits in absolute values along shot-receiver distance (Figure S6b), there is no clear distance-dependent misfit except for some higher misfits up to ~12 ms at 10–30 m distance. The mean misfit is ~1.1 ms (Figure S6b), and the standard deviation of the misfit is ~1.6 ms (Figure S6c).

## 5. Discussion of Field Survey

### 5.1. General Interpretation of the Velocity Model

The mean velocity and vertical velocity gradient calculated from the ensemble solution are shown in Figures 8a and 8b. In order to only focus on the interpretable part of the velocity model, we clip out the area below the deepest seismic raypath, and make transparent the edges of the model where there is no geophone coverage (Figure 9a). We do not attempt to interpret these poorly constrained regions. We want to emphasize again that the mean velocity shown in Figure 8a represents the mean of the posterior ensembles, so when interpreting the velocity structure we should also take into account the model uncertainty (Figure 8c). In addition, in locations that are poorly constrained by data (i.e., low raypath density), THB will tend to retrieve ensemble solutions distributed similar to the prior on the velocity distribution; therefore, the mean model will return to the mean value of the prior velocity range (also see Text S2). This explains the lower

velocity found in the areas below the deepest raypath (white dashed line in Figure 8a). These locations are also characterized by greatest uncertainty, and can therefore easily be identified as uninterpretable.

We can identify several features from the mean velocity and the vertical velocity gradient plots: (1) Below hillslopes and ridgetops, the seismic velocity is commonly lower than 700 m/s (mostly 450 m/s) in the top 1–3 m below surface. This low velocity layer is much thinner or absent below channels. (2) Below this low velocity zone, there is a >10 m thick zone with higher vertical velocity gradient (>200 m/s/m; Figure 8b), and the value of the velocity gradient is higher near the channels. The velocity generally increases from <1,000 to ~3,000 m/s from the top to the bottom of this high velocity gradient layer. (3) Below the high velocity gradient layer, the velocity increases more gradually from ~3,000 to ~4,000 m/s close to the deepest raypath. (4) Although model uncertainty is higher close to the deepest raypaths, the deepest raypaths present as a mirror image of the surface topography (Figure 8).

We estimate the model uncertainty based on the coefficient of variation (Figure 8c) and find variations generally less than 25% within the domain sampled by raypaths. There is higher variation below the channel (MH4) and ridgetop (MH4R), possibly due to a rapid change of velocity, which may indicate the presence of layer boundaries. Uncertainty is also slightly greater below the high velocity gradient layer described in the last paragraph. Below the hillslopes, velocity is lower (yellow-to-brown color) at horizontal distances 100, 130, and 205 m; however, the coefficient of variation corresponding to these regions is also greater. The high variation here indicates greater differences within the THB ensemble, which is likely a result of lesser raypath coverage in these regions (Figure 8d). As a result, the inverted velocity here is not well constrained. The coefficient of variation allows us to interpret the model resolution, but the value itself is not directly equivalent to model accuracy.

As *P*-wave velocity of the shallowest layer is between 450 and ~700 m/s, the material comprising this layer is likely soil near the ground surface trending to a mixture of soil and saprolite with depth. Given our 3 m geophone spacing, we cannot directly determine the thickness of the soil layer due to poorer resolution of the shallowest few meters. Below the top layer, the velocity gradient is commonly greater, with *P*-wave velocity increasing almost linearly from ~700 to ~3,000 m/s, as is highlighted in the velocity gradient plot (Figure 8b). This is even more pronounced especially toward the channels. Laboratory experiments show that depending on the ambient stress and porosity, the *P*-wave velocity of sedimentary rocks in the upper crust generally ranges from 2,000 to 4,000 m/s (Saxena et al., 2018). In particular, the *P*-wave velocity of fresh (not chemically altered) sandstone in shallow crust with 10% or 20% porosity is 4,600 or 3,800 m/s, respectively (Geldart & Sheriff, 2004). We therefore infer that the material comprising this second layer is a mixture of saprolite and weathered bedrock. The increase of seismic velocity here could also be due to reduction of porosity (Hayes et al., 2019; Holbrook et al., 2014) and/or reduction of chemical weathering (e.g., Gu et al., 2020), reflecting an increase of material strength in the saprolite or weathered bedrock materials. Note that this middle layer is thicker (~15 m) below the ridgetops than elsewhere. Below here, seismic velocity increases from ~3,000 to > 4,000 m/s with a lower vertical velocity gradient. The gradual increase of velocity in this layer represents the transition from more weathered (either chemically and/or physically) to more pristine, low porosity bedrock below. However, due to the poorer resolving power of seismic refraction at greater depth, we cannot provide further insights into the abruptness of the transition from weathered to fresh bedrock.

To compare velocity structures at different locations along the survey line, we plot a selection of vertical profiles below ridgetops, hillslopes, and channels, and document the velocity and velocity gradient structures (Figures 9b–9d). In ridgetop profiles (MH3R and MH4R in Figure 9a), velocity increases from 450 m/s near the surface to 3,500 m/s close to 35 m depth, with the standard deviation increasing to ~400 m/s (Figure 9b). However, the velocity structure profile is quite different between ridges MH4R and MH3R. The velocity profile below MH4R rapidly increases to ~3,000 m/s and stays as a constant below 11 m depth. Below hillslopes (Figure 9c), the velocity profiles of 3 locations are nearly identical, with a constant low velocity (450 m/s) for the top 1–2 m, followed by a rapid increase of velocity from 450 to ~3,500 m/s at ~15 m depth, and then nearly constant below, regardless of slope aspect. This finding is different from the strong aspect ratios between north and south facing slopes in the Shale Hills Critical Zone Observatory in Pennsylvania (e.g., West et al., 2019). The standard deviation of velocity is roughly the same below hillslopes and below



ridgetops, indicating similar resolving power. Below channels (Figure 9d), the low velocity layer is absent and the velocity increases to  $\sim 4,000$  m/s at shallower depth with low uncertainty (above 10 m depth).

As demonstrated in the synthetic models A and B, THB inversion is able to detect a sudden increase of velocity (Figure 4), though not able to precisely recover the step increase in velocity gradient as set up in the synthetic models (the green lines in the gradient profiles in Figure 6) due to presence of measurement noise and geophone spacing. Field data indicates that constant velocity layers with velocity jumps, as implemented in models A and B, may not be realistic in Earth structure. In synthetic model C, THB is able to retrieve gradual increases of velocity and changes of velocity gradient (Figures 5 and 6), similar to those found in the velocity profiles shown in the field data inversion. We want to emphasize that in THB inversion we do not impose a model smoothing parameter, so the gradual velocity increase with depth is more likely to be a real structure. The presence of a high velocity gradient zone in our field survey, rather than velocity jumps, implies a lack of sharp material boundaries below hillslopes.

To summarize the field data at Rancho Venada, the seismic velocity model suggests a weathered, unconsolidated material such as soil near the surface, followed by a  $\sim 10$  m thick layer with increasing saprolite component, a weathered bedrock layer with gradually increasing material strength with depth, and unweathered bedrock underneath.

## 5.2. Broader Implications of the CZ Structure at the Study Site

By comparing the vertical velocity gradient and the seismic velocity, we find that when  $V_p < 2,000$  m/s, the highest vertical velocity gradient (black contour line in Figure 9a) roughly coincides with the 1,400 m/s  $V_p$  contour line (dashed white contour line in Figure 9a). This contour line falls within a zone of high velocity gradient, as introduced in Section 5.1, and possibly indicates a more pronounced increase of material competency at the contour depth. From borehole drilling experiments in a granitic site in Laramie Range, Wyoming, Flinchum et al. (2018) observe that the material  $V_p$  is  $\sim 1,200$  m/s near the casing depth at four boreholes. The depth of casing indicates the presence of competent material, which they interpret as the top of weathered bedrock. Although we are not able to determine the process that dominates the strong vertical velocity gradient at Rancho Venada, we find some similarity in near-surface seismic velocity structure between our study site and sites in Laramie Range, Wyoming (Flinchum et al., 2018), southern Sierra Nevada, California (Hayes et al., 2019; Holbrook et al., 2014), Gordon Gulch, Colorado (Befus et al., 2011), and the Shale Hills Critical Zone Observatory (Gu et al., 2020). In this study, saprolite-weathered bedrock is interpreted as between 700 and 3,000 m/s in the layer with high velocity gradient (Section 5.1). The consideration of 3,000 m/s as saprolite material is higher than the saprolite  $P$ -wave velocity reported by Befus et al. (2011), Olyphant et al. (2016), Flinchum et al. (2018), and West et al. (2019) with evidence from drilling. It is therefore also possible that the saprolite-weathered bedrock transition occurs at the highest velocity gradient, near 1,400 m/s. Future drilling at the study site will directly constrain the saprolite-bedrock transition.

Since the strike and dip of the Cretaceous sedimentary bedrock units are near identical in our field site (Figure 2b) and the survey line is parallel to the bedding strike, we can rule out the scenario that the difference in structure below hillslopes versus channels is due to bedrock geometry or change in lithology. Instead, our result suggests that the difference in velocity structure is likely influenced by different weathering processes and conditions between channels and hillslopes. The most significant velocity feature that distinguishes channels from hillslopes is the presence of high velocities ( $> 4,000$  m/s) at shallow depths below channels. This rapid transition from low to high velocity likely indicates a shallower weathering front, while the more gradual increase of velocity below hillslopes implies a thicker, more developed saprolite layer (high vertical velocity gradient layer in Figure 8b) toward ridgetops.

Flinchum et al. (2018) interpret a saprolite, weathered bedrock, and protolith layers in the CZ structure along hillslopes based on seismic refraction and drilling. Toward the ridgetops, they infer a convex up boundary between the saprolite and weathered bedrock layers, and the topography of the protolith is inverted relative to the surface topography (Figure 13 in Flinchum et al., 2018). Based on our field survey at Rancho Venada, the topography of the high velocity gradient zone (the light yellow color in Figure 8b) presents a convex up structure toward ridgetops. On the other hand, the elevation along the deepest raypaths (the white dashed

line in Figure 8) decreases toward ridgetops. Although we are not able to resolve velocity below the deepest raypaths, the higher density of raypaths along the deepest resolvable velocity suggests a sudden increase of velocity. This velocity increase suggests the weathered to unweathered bedrock transition likely mirrors the surface topography. The velocity structure characterized at Rancho Venada is similar to what is found by Flinchum et al. (2018), despite different geology and climate conditions. By solely using active source seismic refraction, the uncertainty and difficulty in identifying material boundaries hinders our capability of testing different CZ hypotheses. Without directly accessing rock material (e.g., drilling), it is challenging to further relate  $V_p$  to specific types of material at our study site. Further investigations including direct assessment to material and sampling are needed to provide better insights into the CZ evolution in our study site.

## 6. Future Work

We rely on  $P$ -wave arrival time picking and seismic refraction for inferring seismic velocity structure. The method and the field configuration designed in this study can also be applied to other near-surface geophysics studies such as ice structure in glaciers (Marusiak et al., 2020; Montgomery et al., 2017), lava layers in volcanic fields (Wells et al., 1985), or the hydrologic structures in floodplains (Steelman et al., 2018). There are other techniques in seismology for imaging subsurface structure such as  $S$ -wave ( $V_s$ ) arrival, surface wave dispersion, seismic reflection, and so on. For example, subsurface moisture content can strongly influence  $P$ -wave velocity (Gregory, 1976). To properly measure fracture density and how much water can be stored within the CZ structure, work related to in situ measurement of soil/rock moisture in different seasons will be essential. Direct borehole drilling through CZ structure and relating core samples to seismic structure (e.g., Flinchum et al., 2018; St. Clair et al., 2015) will provide ground-truth material properties and how they are related to seismic imaging, and therefore a better picture of the evolution of CZ structure in different geologic and climatic conditions. For example, measuring porosity and chemical element depletion along the boreholes and the calibration with the seismic velocity profiles will allow us to estimate porosity, chemical weathering, and volumetric strain based on seismic velocity models (Gu et al., 2020; Hayes et al., 2019; Holbrook et al., 2014).

## 7. Conclusions

In this study, we provide an open source Transdimensional Hierarchical Bayesian inversion scheme for traveltimes measurements made on data from active source seismic refraction experiments. The THB inversion is implemented using reversible-jump Markov Chain Monte Carlo (THB rjMCMC) and is shown to better resolve seismic structure compared to traditional techniques, while eliminating the need for explicit regularization through smoothing. We explore active source seismic refraction fieldwork configurations as well as a novel inversion scheme to better resolve deep critical zone structure. We used three unique 2D synthetic models with different input model geometry to compare the traditional inversion method and THB. Traditional seismic refraction inversions poorly resolve velocity structure boundaries and gradual velocity increases with depth. Additionally, without addressing data and model uncertainties, we cannot rigorously interpret deep critical zone structure. With the THB approach that simultaneously minimizes model misfit and estimates measurement uncertainty, we are able to identify deeper velocity boundaries. Based on active source seismic refraction surveys along the strike of the Cretaceous sedimentary rocks in northern California, the mean velocity model from the field survey data using THB shows that along the survey lines, there is commonly a near constant seismic velocity at shallow depth (0–3 m below ground surface), followed by an increase in velocity (i.e., high velocity gradient) from 700 to 3,000 m/s, and finally a more gradual velocity increase from ~3,000 to > 4,000 m/s. We interpret this velocity structure as transitions from soil, saprolite, and weathered bedrock to unweathered bedrock. This transition is more gradual below ridgetops and hillslopes than below channels, suggesting a more developed weathering zone along ridgetops and hillslopes. Our work demonstrates that THB is an ideal approach for inverting velocity structure from active source seismic refraction surveys and understanding model uncertainty at depth. This work contributes to our ability to reliably image and interpret CZ structure as well as other near-surface geophysics studies.

## Data Availability Statement

The THB code, user guide, and the Vp traveltime picking data are currently being archived on Zenodo (<http://doi.org/10.5281/zenodo.4590999>). The colormap used in most of the figures are based on Crameri (2018) and Greene (2020).

## Acknowledgments

The authors would like to thank the Brown family and the Hemmi family for granting us the access to their properties and also for their encouragement and support for our field work. Doug Dreger, Bill Dietrich, Alex Bryk, Behnaz Hosseini, Daniella Rempe, Ernie Bell, Michelle Pedrazas, Jesse Hahm, David Dralle, Maryn Sanders, Jeng Hann Chong, Alexis Lopez, Amanda Donalson, Margaret Zimmer, and Kerri Johnson provided insightful comments and/or contributed to the early part of the field work. Steve Holbrook and two anonymous reviewers provide insightful comments that significantly improve the quality of the manuscript. The NASA Postdoctoral Program at Jet Propulsion Laboratory, administered by the Universities Space and Research Association through a contract with NASA supported M.-H. Huang for preliminary fieldworks between 2015 and 2017. Part of this work is supported by NSF-EAR2012616 award to M.-H. Huang, a Paglia Post-Bachelor Research Fellow Award to B. Hudson-Rasmussen, and a Packard Foundation Fellowship and NSF-EAR1352214 award to V. Lekic. This study was inspired after participating in a fieldwork led by Bill Dietrich and Steve Holbrook in 2014. *Pickwin* and *Plotrefa* are licensed software developed by Geometrics (<https://www.geometrics.com/>).

## References

- Anderson, R. S., Anderson, S. P., & Tucker, G. E. (2013). Rock damage and regolith transport by frost: An example of climate modulation of the geomorphology of the critical zone. *Earth Surface Processes and Landforms*, 38(3), 299–316. <https://doi.org/10.1002/esp.3330>
- Befus, K. M., Sheehan, A. F., Leopold, M., Anderson, S. P., & Anderson, R. S. (2011). Seismic constraints on critical zone architecture, Boulder Creek watershed, Front Range, Colorado. *Vadose Zone Journal*, 10(4), 1342. <https://doi.org/10.2136/vzj2010.0108er>
- Bodin, T., & Sambridge, M. (2009). Seismic tomography with the reversible jump algorithm. *Geophysical Journal International*, 178(3), 1411–1436. <https://doi.org/10.1111/j.1365-246x.2009.04226.x>
- Bodin, T., Sambridge, M., Rawlinson, N., & Arroucau, P. (2012). Transdimensional tomography with unknown data noise. *Geophysical Journal International*, 189(3), 1536–1556. <https://doi.org/10.1111/j.1365-246x.2012.05414.x>
- Burdick, S., & Lekic, V. (2017). Velocity variations and uncertainty from transdimensional P-wave tomography of North America. *Geophysical Journal International*, 209, 1337–1351. <https://doi.org/10.1093/gji/ggx091>
- Burdick, S., Waszek, L., & Lekic, V. (2019). Seismic tomography of the uppermost inner core. *Earth and Planetary Science Letters*, 528, 115789. <https://doi.org/10.1016/j.epsl.2019.115789>
- Crameri, F. (2018). *Scientific colour-maps*. Zenodo. <http://doi.org/10.5281/zenodo.1243862>
- Dettmer, J., & Dosso, S. E. (2013). Probabilistic two-dimensional water-column and seabed inversion with self-adapting parameterizations. *Journal of the Acoustical Society of America*, 133(5), 2612–2623. <https://doi.org/10.1121/1.4795804>
- Dettmer, J., Molnar, S., Steininger, G., Dosso, S. E., & Cassidy, J. F. (2012). Trans-dimensional inversion of microtremor array dispersion data with hierarchical autoregressive error models. *Geophysical Journal International*, 188, 719–734. <https://doi.org/10.1111/j.1365-246x.2011.05302.x>
- Flinchum, B. A., Steven Holbrook, W., Rempe, D., Moon, S., Riebe, C. S., Carr, B. J., et al. (2018). Critical zone structure under a granite ridge inferred from drilling and three-dimensional seismic refraction data. *Journal Geophysical Research: Earth Surface*, 123, 1317–1343. <https://doi.org/10.1029/2017j004280>
- Galetti, E., & Curtis, A. (2018). Transdimensional electrical resistivity tomography. *Journal of Geophysical Research: Solid Earth*, 123, 6347–6377. <https://doi.org/10.1029/2017JB015418>
- Galetti, E., Curtis, A., Meles, G. A., & Baptie, B. (2015). Uncertainty loops in travel-time tomography from nonlinear wave physics. *Physical Review Letters*, 114(14), 148501. <https://doi.org/10.1103/physrevlett.114.148501>
- Geldart, L. P., & Sheriff, R. E. (2004). *Problems in exploration seismology and their solutions*. Houston, TX: Society of Exploration Geophysicists.
- Greene, C. (2020). *Crameri perceptually uniform scientific colormaps*. MATLAB Central File Exchange. Retrieved from <https://www.mathworks.com/matlabcentral/fileexchange/68546-crameri-perceptually-uniform-scientific-colormaps>
- Green, P. J. (1995). Reversible jump Markov chain Monte Carlo computation and Bayesian model determination. *Biometrika*, 82, 711–732. <https://doi.org/10.1093/biomet/82.4.711>
- Gregory, A. R. (1976). Fluid saturation effects on dynamic elastic properties of sedimentary rocks. *Geophysics*, 41, 895–921. <https://doi.org/10.1190/1.1440671>
- Gu, X., Mavko, G., Ma, L., Oakley, D., Accardo, N., Carr, B. J., et al. (2020). Seismic refraction tracks porosity generation and possible CO<sub>2</sub> production at depth under a headwater catchment. *Proceedings of the National Academy of Sciences of the United States of America*, 117, 18991–18997. <https://doi.org/10.1073/pnas.2003451117>
- Hawkins, R., Bodin, T., Sambridge, M., Choblet, G., & Husson, L. (2019). Trans-dimensional surface reconstruction with different classes of parameterization. *Geochemistry, Geophysics, Geosystems*, 20(1), 505–529. <https://doi.org/10.1029/2018GC008022>
- Hayes, J. L., Riebe, C. S., Holbrook, W. S., Flinchum, B. A., & Hartsough, P. C. (2019). Porosity production in weathered rock: Where volumetric strain dominates over chemical mass loss. *Science Advances*, 5, eaao0834. <https://doi.org/10.1126/sciadv.aao0834>
- Holbrook, W. S., Riebe, C. S., Elwaseif, M., L. Hayes, J. J., Basler-Reeder, K., L. Harry, D., et al. (2014). Geophysical constraints on deep weathering and water storage potential in the Southern Sierra Critical Zone Observatory. *Earth Surface Processes and Landforms*, 39, 366–380. <https://doi.org/10.1002/esp.3502>
- Julian, B. R., & Gubbins, D. (1977). Three-dimensional seismic ray tracing. *Journal of Geophysics*, 43, 95–113.
- Kroon, D. J. (2021). *Accurate fast marching*. MATLAB Central File Exchange. Retrieved from <https://www.mathworks.com/matlabcentral/fileexchange/24531-accurate-fast-marching>
- Lebedeva, M. I., & Brantley, S. L. (2013). Exploring geochemical controls on weathering and erosion of convex hillslopes: Beyond the empirical regolith production function. *Earth Surface Processes and Landforms*, 38(15), 1793–1807. <https://doi.org/10.1002/esp.3424>
- Lindsay, J. B. (2006). Sensitivity of channel mapping techniques to uncertainty in digital elevation data. *International Journal of Geographical Information Science*, 20(6), 669–692. <https://doi.org/10.1080/13658810600661433>
- Malinverno, A. (2002). Parsimonious Bayesian Markov chain Monte Carlo inversion in a nonlinear geophysical problem. *Geophysical Journal International*, 151(3), 675–688. <https://doi.org/10.1046/j.1365-246x.2002.01847.x>
- Malinverno, A., & Briggs, V. A. (2004). Expanded uncertainty quantification in inverse problems: Hierarchical Bayes and empirical Bayes. *Geophysics*, 69(4), 1005–1016. <https://doi.org/10.1190/1.1778243>
- Marusiak, A. G., Schmerr, N. C., DellaGiustina, D. N., Pettit, E. C., Dahl, P. H., Avenson, B., et al. (2020). The deployment of the seismometer to investigate ice and ocean structure (SIIOS) on Gulkana Glacier, Alaska. *Seismological Research Letters*, 91, 1901–1914. <https://doi.org/10.1785/0220190328>
- Menke, W. (1984). *Geophysical data analysis: Discrete inverse theory*. Cambridge, MA: Academic Press, Inc.
- Metropolis, N., Rosenbluth, A. W., Rosenbluth, M. N., Teller, A. H., & Teller, E. (1953). Equation of state calculations by fast computing machines. *The Journal of Chemical Physics*, 21, 1087–1092. <https://doi.org/10.1063/1.1699114>
- Montgomery, L. N., Schmerr, N., Burdick, S., Forster, R. R., Koenig, L., Legchenko, A., et al. (2017). Investigation of firn aquifer structure in southeastern Greenland using active source seismology. *Frontiers of Earth Science*, 5. <https://doi.org/10.3389/feart.2017.00010>

- National Research Council (NRC). (2001). *Basic research opportunities in earth science*. Washington, DC: The National Academies Press.
- Nelson, M. D., Bryk, A. B., Fauria, K., Huang, M.-H., & Dietrich, W. E. (2017). *Physical properties of shallow landslides and their role in landscape evolution investigated with ultrahigh-resolution lidar data and aerial imagery* (pp. 11–15). New Orleans, LA: AGU.
- Olugboji, T. M., Lekic, V., & McDonough, W. (2017). A statistical assessment of seismic models of the U.S. continental crust using Bayesian inversion of ambient noise surface wave dispersion data. *Tectonics*, 36, 1232–1253. <https://doi.org/10.1002/2017TC004468>
- Olyphant, J., Pelletier, J. D., & Johnson, R. (2016). Topographic correlations with soil and regolith thickness from shallow-seismic refraction constraints across upland hillslopes in the Valles Caldera, New Mexico. *Earth Surface Processes and Landforms*, 41(12), 1684–1696. <https://doi.org/10.1002/esp.3941>
- Pasquet, S., Holbrook, W. S., Carr, B. J., & Sims, K. W. W. (2016). Geophysical imaging of shallow degassing in a Yellowstone hydrothermal system. *Geophysical Research Letters*, 43, 12027–12035. <https://doi.org/10.1002/2016GL071306>
- Peyre, G. (2020). *Toolbox fast marching*. MATLAB Central File Exchange. Retrieved from <https://www.mathworks.com/matlabcentral/fileexchange/6110-toolbox-fast-marching>
- Peyre, G., & Cohen, L. (2004). *Surface segmentation using geodesic centroidal tessellation* (pp. 995–1002). Proceedings of 2nd International Symposium on 3D Data Processing, Visualization and Transmission, 3DPVT 2004, Thessaloniki, Greece.
- Piana Agostinetti, N., Giacomuzzi, G., & Malinverno, A. (2015). Local three-dimensional earthquake tomography by trans-dimensional Monte Carlo sampling. *Geophysical Journal International*, 201(3), 1598–1617. <https://doi.org/10.1093/gji/ggv084>
- Rawlinson, N., & Sambridge, M. (2005). The fast marching method: An effective tool for tomographic imaging and tracking multiple phases in complex layered media. *Exploration Geophysics*, 36, 341–350. <https://doi.org/10.1071/eg05341>
- Ray, A., Kaplan, S., Washbourne, J., & Albertin, U. (2018). Low frequency full waveform seismic inversion within a tree based Bayesian framework. *Geophysical Journal International*, 212(1), 522–542. <https://doi.org/10.1093/gji/ggx428>
- Ray, A., Key, K., Bodin, T., Myer, D., & Constable, S. (2014). Bayesian inversion of marine CSEM data from the Scarborough gas field using a transdimensional 2-D parametrization. *Geophysical Journal International*, 199(3), 1847–1860. <https://doi.org/10.1093/gji/ggu370>
- Ray, A., & Myer, D. (2019). Bayesian geophysical inversion with trans-dimensional Gaussian process machine learning. *Geophysical Journal International*, 217(3), 1706–1726. <https://doi.org/10.1093/gji/ggz111>
- Rempe, D. M., & Dietrich, W. E. (2014). A bottom-up control on fresh-bedrock topography under landscapes. *Proceedings of the National Academy of Sciences of the United States of America*, 111, 6576–6581. <https://doi.org/10.1073/pnas.1404763111>
- Rich, E. I. (1971). *Geologic map of the Wilbur Springs quadrangle, California (Map I-538)*. Retrieved from [https://ngmdb.usgs.gov/Prodesc/proddesc\\_444.htm](https://ngmdb.usgs.gov/Prodesc/proddesc_444.htm)
- Riebe, C. S., Hahm, W. J., & Brantley, S. L. (2017). Controls on deep critical zone architecture: a historical review and four testable hypotheses. *Earth Surface Processes and Landforms*, 42, 128–156. <https://doi.org/10.1002/esp.4052>
- Ryberg, T., & Haberland, C. (2018). Bayesian inversion of refraction seismic traveltime data. *Geophysical Journal International*, 212, 1645–1656. <https://doi.org/10.1093/gji/ggx500>
- Sambridge, M., Gallagher, K., Jackson, A., & Rickwood, P. (2006). Trans-dimensional inverse problems, model comparison and the evidence. *Geophysical Journal International*, 167(2), 528–542. <https://doi.org/10.1111/j.1365-246x.2006.03155.x>
- Saxena, V., Krief, M., & Adam, L. (2018). *Handbook of borehole acoustics and rock physics for reservoir characterization*. Amsterdam, The Netherlands: Elsevier.
- Sethian, J. A. (1996). A fast marching level set method for monotonically advancing fronts. *Proceedings of the National Academy of Sciences of the United States of America*, 93(4), 1591–1595. <https://doi.org/10.1073/pnas.93.4.1591>
- St. Clair, J., Moon, S., Holbrook, W. S., Perron, J. T., Riebe, C. S., Martel, S. J., et al. (2015). Geophysical imaging reveals topographic stress control of bedrock weathering. *Science*, 350, 534–538. <https://doi.org/10.1126/science.aab2210>
- Steelman, C. M., Arnaud, E., Pehme, P., & Parker, B. L. (2018). Geophysical, geological, and hydrogeological characterization of a tributary buried bedrock valley in southern Ontario. *Canadian Journal of Earth Sciences*, 55, 641–658. <https://doi.org/10.1139/cjes-2016-0120>
- Tarantola, A., & Valette, B. (1982). Generalized nonlinear inverse problems solved using the least squares criterion. *Reviews of Geophysics*, 20, 219–232. <https://doi.org/10.1029/rg020i002p00219>
- Visser, G., Guo, P., & Saygin, E. (2019). Bayesian transdimensional seismic full-waveform inversion with a dipping layer parameterization. *Geophysics*, 84(6), R845–R858. <https://doi.org/10.1190/geo2018-0785.1>
- Wells, S. G., Dohrenwend, J. C., McFadden, L. D., Turrin, B. D., & Mahrer, K. D. (1985). Late Cenozoic landscape evolution on lava flow surfaces of the Cima volcanic field, Mojave Desert, California. *GSA Bulletin*, 96, 1518–1529. [https://doi.org/10.1130/0016-7606\(1985\)96<1518:LCLEOL>2.0.CO;2](https://doi.org/10.1130/0016-7606(1985)96<1518:LCLEOL>2.0.CO;2)
- West, N., Kirby, E., Nyblade, A. A., & Brantley, S. L. (2019). Climate preconditions the Critical Zone: Elucidating the role of subsurface fractures in the evolution of asymmetric topography. *Earth and Planetary Science Letters*, 513, 197–205. <https://doi.org/10.1016/j.epsl.2019.01.039>